CTFFIND5 provides improved insight into quality, tilt and thickness of TEM samples

Johannes Elferich [a, b,*], Lingli Kong [a], Ximena Zottig [a,b], Nikolaus Grigorieff [a,b,*]

[a] RNA Therapeutics Institute, University of Massachusetts Chan Medical School RNA Therapeutics Institute

[b] Howard Hughes Medical Institute

[*] Correspondence: *johannes.elferich@umassmed.edu*, *niko@grigorieff.org*

Abstract

Images taken by transmission electron microscopes are usually affected by lens aberrations and image defocus, among other factors. These distortions can be modeled in reciprocal space using the contrast transfer function (CTF). Accurate estimation and correction of the CTF is essential for restoring the high-resolution signal in cryogenic electron microscopy (cryoEM). Previously, we described the implementation of algorithms for this task in the *cis*TEM software package (Grant et al., 2018). Here we show that taking sample characteristics, such as thickness and tilt, into account can improve CTF estimation. This is particularly important when imaging cellular samples, where measurement of sample thickness and geometry derived from accurate modeling of the Thon ring pattern helps judging the quality of the sample. This improved CTF estimation has been implemented in CTFFIND5, a new version of the *cis*TEM program CTFFIND. We evaluated the accuracy of these estimates using images of tilted aquaporin crystals and eukaryotic cells thinned by focused ion beam milling. We estimate that with micrographs of sufficient quality CTFFIND5 can measure sample tilt with an accuracy of 3° and sample thickness with an accuracy of 5 nm.

Introduction

Transmission electron microscopy of biological specimens at cryogenic temperatures (cryoEM) has become a widely used method to image biomolecules at high resolution, both in solution and within the cell. To retrieve the high-resolution signal, the cryoEM images have to be corrected for the contrast-transfer function (CTF) of the microscope. Common parameters used to describe the CTF include an astigmatic defocus, the spherical aberration of the objective lens, and if appropriate, a phase shift introduced by a phase plate. The defocus and phase shift parameters are commonly estimated by fitting the Thon ring pattern (Thon, 1971) in the power spectrum of micrographs to a modeled power spectrum. The program CTFFIND4 (Rohou and Grigorieff, 2015) has been developed for this task and the model and conventions to describe the CTF are widely adopted in the field.

A limitation of CTFFIND4 is that it considers the whole imaged sample to be at the same objective defocus, which is a reasonable assumption for flat and thin samples, as is common in single-particle cryoEM. However, the increased thickness of cryoEM samples of cells may introduce additional modulations in the Thon ring pattern (Tichelaar et al., 2020) that can lead to errors in the CTF modeling when not accounted for. Furthermore, samples of cells are often tilted with respect to the optical axis of the microscope, either unintentionally due to thinning methods such as cryogenic focused ion beam (FIB) milling, or intentionally during electron cryo-tomography imaging. In both cases the effects are strongest at high-resolution, where the Thon rings are more tightly spaced.

Here we describe new features of CTFFIND5 that can fit the modulations of the Thon ring patterns and determine sample thickness and tilt using an extended CTF model with additional parameters. This not only increases the fidelity of the fit, as Thon rings at higher resolution can now be fitted reliably, but also gives valuable insight into the geometry of the sample that can aid the experimentalist.

Methods

Tilt estimation algorithm

Tilt estimation in CTFFIND5 follows a strategy that is similar to the implementation in CTFTILT (Mindell and Grigorieff, 2003). The tilt axis direction ϕ and tilt angle θ are determined by fitting Thon ring patterns locally, calculated from 128 x 128 pixel tiles that form a regular grid covering the micrograph (Fig. 1a). In this model, ϕ has a positive value ranging from 0° to 360° and describes the angle of the tilt axis to the X axis of the micrograph in the counterclockwise direction. The tilt angle θ has positive values ranging from 0° to 90° and describes the rotation of the sample around the tilt-axis in a counterclockwise direction. It is assumed that the defocus variation across the sample can be described by a tilted plane. Fits are evaluated using correlation coefficients between modeled CTFs and Thon ring patterns. Initially, the micrograph pixel size is adjusted (binned) by Fourier cropping to match the resolution limit of the fit set by the user and the micrograph is cropped to be square in order to speed up computation. A power spectrum is calculated from this binned and cropped image, a smooth background is calculated using a box convolution (Mindell and Grigorieff, 2003) and subtracted, the power spectrum is further binned to the tile size (128 x 128 pixels), and the fit of the tilted Thon ring patterns across the micrograph is initialized by fitting this highly binned power spectrum with a non-astigmatic CTF. This fit is then refined using a two-dimensional CTF with astigmatism. Rough values for the tilt axis and angle are then determined in a systematic search in 10° and 5°, respectively, using the locally fitted Thon ring patterns to score each pair of tilt axis and angle, followed by local refinement of tilt axis, angle and average defocus.

Finally, an average tilt-corrected power spectrum at a tile size requested by the user (usually 512 x 512 pixels) is calculated for diagnostic purposes and for further refinement of CTF parameters. The tilt correction is designed to remove most of the Thon ring blurring due to the defocus variation across the image. To minimize ring blurring, the power spectrum from each tile is adjusted according to its local average defocus, $\Delta f_{average}$, by magnifying it by a factor m with

$$m = \sqrt{\Delta f_{local} / \Delta f_{average}} \qquad (1)$$

Since Δf_{local} will assume values across the image that are both smaller and larger than $\Delta f_{average}$, m will assume values smaller and larger than 1. The magnification / demagnification of the power spectrum compensates for the contraction / expansion of the Thon rings due to the local defocus change and produces approximately constant Thon ring patterns that can be averaged without losing the pattern (Fig. 1b). The compensation will have a small error if the spherical aberration is not zero. However, this error is sufficiently small to not visibly affect the Thon rings in the average.

Verification of tilt estimation using tilted aquaporin crystals

To test the robustness and accuracy of the new fitting algorithm, the defocus and sample tilts of aquaporin 2D crystals (Murata et al., 2000) were estimated using a search range from 5000 Å to 50000 Å and a 100 Å step, low and high resolution limits of 30 Å to 5 Å, respectively, and a box size for the final power spectrum of 512 pixels. The estimated tilt angle θ and axis direction ϕ were compared with the values obtained by 2D crystallographic processing (Mindell and Grigorieff, 2003).

Verification of tilt estimation using tilt series

Lamellae prepared from ER-HoxB8 cells were imaged using a Titan Krios 300 keV TEM controlled by SerialEM (Mastronarde, 2005). For each dataset, an initial exposure was taken with a magnification of 64,000, resulting in a pixel size of 1.6 Å and an exposure of 30 $e^-/Å^2$. This was followed by the acquisition of a tilt series at a magnification of 48,000, resulting in a pixel size of 2.087 Å. A total of 35 tilt images at a tilt interval of 3° were collected from -51° to 51°, relative to the milling angle, using a grouped dose-symmetric scheme (Hagen et al., 2017). The exposure per tilt was 3 $e^-/Å^2$, resulting in a total exposure of 105 $e^-/Å^2$.

Lamellae prepared by FIB milling usually exhibit a pre-tilt with respect to the grid surface due to the stage tilt in the FIB instrument. In the microscope, the direction of this pre-tilt will generally not line up with the goniometer tilt axis. For the alignment of a tomogram recorded from such a lamella, the relative orientation of these two axes will have to be determined, together with the precise amount of pre-tilt. We wrote a new *cis*TEM (Grant et al., 2018) program, called fit_tilt_model, to read the tilt angles and axes determined for each image in a tomographic tilt series and fit them to a model incorporating a pre-tilt and a single tomographic tilt axis. Using a rotation matrix R_0 to represent the pre-tilt and rotation matrices R_{tom}^i to represent the tomographic tilt angles and axis read from the microscope, the overall sample orientations are given by

$$R^i = R_0 \times R_{tom}^i \qquad (2)$$

R_0 and R_{tom}^i are calculated from the tilt angles θ and axes ϕ as

$$R = \begin{bmatrix} \cos(\phi)^2 + \sin(\phi)^2 \cos(\theta) & \cos(\phi)\sin(\phi)\,(\cos(\theta) - 1) & -\sin(\phi)\sin(\theta) \\ \cos(\phi)\sin(\phi)\,(\cos(\theta) - 1) & \cos(\phi)^2 \cos(\theta) + \sin(\phi)^2 & -\cos(\phi)\sin(\theta) \\ \sin(\phi)\sin(\theta) & \cos(\phi)\sin(\theta) & \cos(\theta) \end{bmatrix} \qquad (3)$$

Using the tilt information obtained with CTFFIND5, we now have a set of rotation matrices R^i, and together with the rotation matrices read from the microscope, R_{tom}^i, we can calculate a set of pre-tilt estimates R_0^i from Eq. (2). To determine the best overall pre-tilt R_0, we determine the plane-normal vectors $V_{norm}^i = [x, y, z]$ of the sample by applying R_0^i to the vector [0,0,1] (z-coordinate along the beam direction), followed by calculating their mean $V_{norm}^{mean} = [x_o,\ y_0,\ z_0]$ as the normal vector of the best overall pre-tilt estimate. By calculating the root mean squared deviation of the normal vectors V_{norm}^i, outliers can be identified and excluded to further refine V_{norm}^{mean}. The pre-tilt can then be determined as:

$$\theta_0 = \begin{cases} \cos^{-1}(z_0) & x_0 \geq 0 \\ -\cos^{-1}(z_0) & x_0 < 0 \end{cases}$$

$$\phi_0 = \begin{cases} \tan^{-1}(\frac{x_0}{y_0}) & y_0 \neq 0, \phi_0 \in [0°, 180°] \\ 90° & y_0 = 0 \end{cases} \quad (4)$$

To generate more reliable defocus and tilt estimates, the defocus search range and resolution fitting range can be adjusted according to the experimental tilt range and image quality. For our cryoEM samples, the low and high resolution limits were set to 50 Å to 10 Å, respectively, and the defocus search interval was set to be between $\pm$ 10000 and $\pm$20000 Å from the nominal defocus set during data collection.

Sample thickness estimation

In CTFFIND5 we implemented a new CTF_t model function, based on the CTF function implemented in CTFFIND4 (Rohou and Grigorieff, 2015) and extended by the formula described by (McMullan et al., 2015):

$$CTF_t(\lambda, \mathrm{g}, \Delta f, C_s, \Delta\varphi, \omega_2, t) = \frac{1}{2}\Big(1 - \mathrm{sinc}\big(\xi(\lambda, \mathrm{g}, t)\big)\cos\big(2\chi(\lambda, |\mathrm{g}|, \Delta f, C_s, \Delta\varphi, \omega_2)\big)\Big) \quad (5)$$

where χ denotes the phase-shift as a function of the electron wavelength λ, the spatial frequency vector |g|, the objective defocus Δf, the spherical aberration C_s, the additional phase shift $\Delta\varphi$, and the fraction of amplitude contrast ω_2. The modulation of the CTF due to sample thickness t is described by the function sinc(ξ) with ξ defined as:

$$\xi(\lambda, \mathrm{g}, t) = \pi\lambda \mathrm{g}^2 t \quad (6)$$

This sinc modulation envelope (Fig. 3a) attenuates the amplitude of the Thon rings with increasing spatial frequencies and produces nodes where the apparent amplitude is zero

(Tichelaar et al., 2020). After the first node the thon rings appear "inverted" compared to the CTFFIND4 CTF model, with maxima in the thon rings appearing where the CTF model is 0. This causes the quality of fit indicator to rapidly decrease at the first node in CTFFIND4. The location of the first node is marked with a # in Fig. 3a.

If a user requests sample thickness estimation, the program will first fit the CTF model function as implemented in CTFFIND4. If the user also requested tilt estimation the tilt corrected power spectrum will be used for all subsequent steps. Initially, the "goodness of fit" resolution g_{GoF} will be used as an estimate for the frequency of the first node of the CTF_t function, which occurs when the sinc term in Eq. 5 becomes 0 for the first time at $\xi = \pi$. By setting $\xi = \pi$ in Eq. 6, we can obtain an estimate of the sample thickness t, from g_{GoF}:

$$t = {}^{1}/_{\lambda g_{GoF}{}^{2}} \qquad (7)$$

If the option "Brute-force 1D fit" is selected, CTFFIND5 will further refine t and Δf by calculating the normalized cross-correlation between the radial average of the power spectrum, corrected for astigmatism by EquiPhase Averaging (EPA) as described in (Zhang, 2016), and CTF_t, searching systematically for the best combination of t in the range of 50-400 nm in 10 nm steps, and Δf in the range of $\pm$200 nm from the previously fitted value, also in 10 nm steps.

Finally, if the option "2D-refinement" is selected, CTFFIND5 will optimize t, Δf_1, Δf_2, and ω using the same conjugate gradient algorithm used in CTFFIND4 and the normalized cross correlation between CTF_t and the 2D power spectrum as a scoring function.

After the optimal values for t and Δf have been obtained the "goodness of fit" crosscorrelation is recalculated using CTF_t, with a frequency window that is 1.5 times larger than in CTFFIND4 to avoid the drop-off in the node regions of CTF_t. For visualization, the astigmatism-corrected 1D power spectrum is displayed as oscillating

around 0.5, as opposed to the default procedure in CTFFIND4, where the minima are scaled to 0. This is done to allow a better visual comparison to the CTF_t model.

Verification of sample thickness estimation using the Beer-Lambert law

We used 655 micrographs collected from one lamella of ER-HoxB8 cells (dataset $\text{Lamella}_{EUC}1$ from (Elferich et al., 2022). For each micrograph we calculated $ln\left(\frac{I}{I_0}\right)$, where I was the sum of all pixels in the illuminated area of the movie and I_0 was the average of this sum for 45 micrographs collected over vacuum with the same energy filter settings. This value is expected to have a linear relationship with the thickness of the sample consistent with the Beer-Lambert law (Rice et al., 2018; Yan et al., 2015):

$$ln\left(\frac{I}{I_0}\right) = \frac{1}{\kappa}t \qquad (8)$$

where κ is the apparent mean free path for inelastic scattering.

We then used CTFFIND5 to estimate the thickness t of each micrograph using the "Brute-force 1D fit" and "2D-refinement" setting, low and high resolution limits set to 30 Å and 5 Å, defocus search range set between 500 nm and 5000 nm, and low and high resolution limits for thickness estimation set to 10 Å and 3 Å. We used a "RANSAC" algorithm as implemented by the scikit-learn Python package (Pedregosa et al., 2011) to fit a linear model to the relationship of $ln\left(\frac{I}{I_0}\right)$ and t, while rejecting outliers. We then manually inspected every outlier of the model fit and categorized the reason for the discrepancy into "Occluded beam" (either from contamination or the edges of the lamella), "Low image signal" (in most cases exposures containing no cellular features), "Carbon/Platinum", and "Lipid droplet" (see Fig. 4).

203 **Verification of sample thickness estimation using tomography**

204 The same tilts series described in the section "Verification of tilt estimation using tilt
205 series" were used here. For tomographic reconstruction, tilt movie frame motion
206 correction was performed using SerialEM (Mastronarde, 2005), and tilt series were aligned
207 using the IMOD software package (version 4.11, (Mastronarde and Held, 2017)). For coarse
208 alignment, a high-frequency cutoff radius of 0.15 was used. A fiducial model was generated
209 using patch tracking with patches of 450 x 450 pixels and a fractional overlap of patches of
210 0.33 x 0.33. High-tilt frames were omitted while generating the fiducial model. Robust
211 fitting with a tuning factor of 1 was used for fine alignment. After computing the alignment,
212 the fiducial model was edited by removing unreliable patches, and then alignments were
213 re-computed. The edited models with the lowest residual mean errors and standard
214 deviations were used for fine alignment. Tomogram positioning was used to correct the tilt
215 angle offset. Fully aligned stacks were generated with a binning factor of 4, resulting in a
216 tomogram pixel size of 8.3 Å. Tomograms were reconstructed using the SIRT-like filtering
217 option in IMOD (Mastronarde, 1997; Mastronarde and Held, 2017) and manually inspected.
218 The tomograms were back-projected along the y-axis using a homemade script, generating
219 a small set of XZ projections. Thickness measurements on the projected central slices were
220 performed using the display program included with the *cis*TEM software package (Grant et
221 al., 2018).

222 **CTF correction of medium magnification lamella images**

223 The CTF of the representative medium magnification image with a pixel size of 40 Å was
224 estimated using CTFFIND5 with the following parameters: defocus range: 1,000,000 to
225 4,000,000 Å; search step 50,000 Å; low and high resolution limits: 400 Å and 80 Å. We then
226 used the program apply_ctf, included with *cis*TEM, to flip the phases according to the
227 estimated CTF. We furthermore implemented the Wiener-like filter described in (Tegunov
228 and Cramer, 2019) in apply_ctf to produce the image shown in Fig. 6d.

229 **Benchmarking CTFFIND5 runtimes**

230 CTFFIND5 runtimes were measured using 3 representative micrographs (Table 2). As a
231 baseline measurement, CTFFIND5 was run without estimation of tilt and sample thickness
232 enabled. Then runtime was measured enabling either one of these options or both. Every
233 test was repeated four times and the average and standard deviation of the last three runs
234 are reported, to minimize the contribution of hard-drive speed. The tests were performed
235 on a single core of an Intel Core i9-12900KF CPU.

236 Results

237 **Tilt estimation**

238 We tested the tilt correction for the Thon rings on a representative micrograph taken from
239 a cryo-FIB milled lamella. As expected, the correction results in the observation of Thon
240 rings at higher spatial resolution (Fig. 1c). In this example, correcting for the estimated
241 moderate tilt of 12.3° improved the highest resolution at which a reasonable fit could be
242 obtained from 5.9 Å to 4.6 Å. The power spectrum also appears less noisy, which can be
243 attributed to some low-pass filtering that occurs with the interpolation of the Thon ring
244 patterns of individual tiles to perform the tilt correction.

245 To test the performance of the new CTFFIND5 sample tilt estimation, we used a dataset of
246 images of tilted aquaporin crystals that were also used to benchmark the original CTFTILT
247 implementation (Mindell and Grigorieff, 2003; Murata et al., 2000). Table 1 compares the
248 tilt information of the samples obtained from crystallographic analysis and the estimates
249 obtained using CTFFIND5. Overall, the results of CTFFIND5 agree well with the aquaporin
250 crystals information. The average discrepancy was 1.9° for the tilt axis direction and 1.5°
251 for the tilt angle.

252 To test whether CTFFIND5 would be able to correctly assign tilt axis and angle for tilt
253 series data, we analyzed two tilt series from different grids of lamellae prepared by cryo-
254 FIB milling from mouse neutrophil-like cells (Elferich et al., 2022). We then plotted the
255 estimated values for tilt axis and angle as a function of nominal stage tilt (Fig. 2). The

256 estimated tilt angle shows a roughly linear relationship with the nominal stage tilt, but
257 since CTFFIND5 reports only positive tilt angles the overall plot has a V-shape. The
258 estimated tilt axis angle is approximately constant at high tilts but changes by about 180° at
259 0° estimated tilt, again due to the convention enforced by CTFFIND5. Notably, in both
260 examples there is an offset of about 20° between nominal and estimated tilts, which is due
261 to the pre-tilt of the specimen caused by FIB-milling at a shallow angle. To quantify and
262 delineate both the tilt axis direction of the microscope and the pre-tilt of the specimen we
263 fit all values to a model as described in Methods (Fig. 2). The fitting resulted in an
264 estimated tilt axis angle of 178.2° and 179.8°, respectively, which is consistent with the
265 SerialEM calibration of 178.4° and 176.3° for the stage tilt axis. The estimated pre-tilt
266 values were 20.6 °and -21.9°, consistent with a FIB-milling angle of 20° and opposite
267 orientation of the grids relative to the milling direction. The pre-tilt axis angles were
268 estimated as 171.8° and 183.8°, which is consistent with the error expected from manually
269 aligning the milling direction when inserting grids into the microscope.

270 To estimate the accuracy of the tilt estimation in tilt series, we calculated the mean absolute
271 difference between the tilt and axis-angle estimates and the fitted model, excluding the axis-
272 angle estimates at tilt angles under 5°. For the first tilt series we obtained accuracy estimates
273 of 2.08° and 2.58° for tilt and axis-angles, respectively. In the second tilt series the accuracy
274 estimates were 3.95° and 9.47°. In both cases the accuracy was lower than for the tilted
275 aquaporin crystals, presumably due to the relatively short exposure of each micrograph in
276 the tilt series. However, the substantially higher mean differences in the second tilt series
277 suggest that the accuracy is highly dependent on the quality of the underlying data.

278 **Sample thickness estimation**

279 Even after correcting for sample tilt we found that for FIB-milled samples we often could
280 observe Thon-ring like modulation in the power spectrum at higher resolution than
281 suggested by the goodness of fit estimate (Fig. 3b, top plot). These modulations are out of
282 phase with the predicted modulations, as described by (McMullan et al., 2015) and
283 (Tichelaar et al., 2020). We therefore implemented an extension of the CTF model as
284 described by (McMullan et al., 2015) (Fig. 3a). For some images we found that the thickness

285 could be well estimated by assuming that the goodness of fit resolution estimate obtained
286 using the old model implemented in CTFFIND4 corresponds to the first node in the
287 modulation function, according to Eq. (7). With our new model, estimated CTF parameters
288 were very similar to those from CTFFIND4, but the fit in CTFFIND5 extended to higher
289 resolution (Fig. 3b).

290 In other images, mostly with defocus values under 1 μm and with a sample thickness over
291 200 nm, CTFFIND4 could fit the power spectrum before and after the first node using the
292 old CTF model, with some deviations between the fit and the power spectrum (Fig. 3c).
293 Fitting the power spectrum with the new model in CTFFIND5 resulted in substantially
294 different estimated CTF parameters and an improved fit, even though the goodness-of-fit
295 estimation did not change. We also found that for some single-particle datasets of large
296 particles, such as the rotavirus double-layered particle (Grant and Grigorieff, 2015), we
297 could use CTFFIND5 to estimate the thickness of the sample, which resulted in CTF fits to
298 higher resolution (Fig. 3d).

299 Based on these results we conclude that CTFFIND5 will provide more accurate CTF
300 parameters for images of thick samples, such as those generated from FIB-milling. In
301 addition, the fit provides a direct readout of the specimen thickness, which is important for
302 judging specimen quality and the potential for high-resolution information that can be
303 recovered from these images.

304 Estimating the accuracy of sample thickness estimation using the Beer-Lambert law 305 on energy filtered data

306 CryoEM is frequently performed using an energy filter to remove inelastically scattered
307 electrons. The fraction of inelastically scattered electrons can be described by the Beer-
308 Lambert law, which states that the fraction of electrons removed from the image is
309 proportional to the thickness of the sample. The apparent mean free path for electron
310 scattering has been experimentally determined for common cryoEM conditions (Rice et al.,
311 2018). To test whether thickness estimation in CTFFIND5 is consistent with this method
312 we used a dataset of 655 exposures of a lamella of ER-HoxB8 cells collected using the DeCo-

313 LACE approach (Elferich et al., 2022). We used CTFFIND5 to estimate the thickness t of
314 every exposure and plotted $-ln\left(\frac{I}{I_0}\right)$ against t (Fig. 4). Fitting the data to a linear model
315 described in Methods (Eq. (8)), we found that 568 out of 655 exposures followed closely a
316 linear relationship with a mean free path κ of 317 nm. Manual inspection of images that did
317 not follow this linear relationship revealed that they either contained visible ice
318 contamination, platinum deposits, or they were collected over ice without cellular features
319 and displayed weak Thon rings. The value of κ is consistent the value found by (Rice et al.,
320 2018), even though our dataset was collected without an objective aperture. The x-axis
321 intercept of the linear model was -14.1 nm, meaning that the node position systematically
322 predicts a smaller thickness than predicted by the Beer-Lambert law. This discrepancy is
323 further discussed in the next section. To estimate the accuracy of the sample thickness
324 determined by CTFFIND5 we calculated the mean absolute difference to the linear model,
325 which was 4.8 nm. These data suggest that sample thickness determination using node-
326 fitting is an alternative to using the Beer-Lambert law that has the advantage of not relying
327 on the constant κ and the intensity I_0, both of which might not be readily available. Also,
328 the two approaches are complementary as they rely on orthogonal mechanisms.

329 **Estimating the accuracy of sample thickness estimation using tomography**

330 We used a dataset of seven micrographs collected from lamellae of ER-HoxB8 cells together
331 with tilt series collected afterwards from the same locations to verify the accuracy of the
332 thickness estimates obtained using CTFFIND5. We used CTFFIND5 to estimate the
333 thickness ($t_{CTFFIND}$) for every location and compared it with the thickness estimated from
334 the tomogram reconstructed from the tilt series (t_{TOMO}). We measured t_{TOMO} by manually
335 estimating the distance between the surfaces of the lamella in three different positions.
336 When we plotted $t_{CTFFIND}$ against t_{TOMO} we found that the values were highly correlated,
337 but t_{TOMO} was consistently smaller than $t_{CTFFIND}$ (Fig. 5). A linear fit revealed a slope of
338 0.95 and a y-axis intercept of 0.12 nm. This means that the CTFFIND5 thickness estimate is
339 on average 1.05x higher than the thickness estimated by tomography. (Tichelaar et al.,
340 2020) also report that estimating the thickness from the CTF nodes resulted in values
341 roughly 1.1x higher than estimated by tomography. The reasons for the systematic

342 discrepancies between thicknesses estimated by CTFFIND5 and estimates based on the
343 Beer-Lambert law and tomography are unclear, but since they are small and CTFFIND5
344 estimates lie in between the other two estimates, they will provide comparable
345 information.

346 **CTF estimation and correction assists biological interpretation of intermediate-**
347 **magnification lamella images**

348 During data collection of cryoEM data in cells, the operator frequently relies on images
349 taken at low magnification to select areas of interest and establish their biological context.
350 The pixel size of these images is usually about 40 Å, with a defocus of about 200 µm. This
351 produces strong contrast from biological membranes but can sometimes also lead to
352 substantial fringes near these membranes (Fig. 6a). We found that a simple CTF correction
353 based on CTFFIND defocus estimates obtained from the overview images can reduce these
354 fringes (Fig. 6b). A simple CTF correction can be done using the program apply_ctf,
355 included with *cis*TEM, by phase flipping according to the fitted CTF (Fig. 6c). However, we
356 found that including a Wiener filter-based amplitude correction described by (Tegunov and
357 Cramer, 2019) produces a more naturally looking image that might be best suited to
358 recognize cellular features (Fig. 6d).

359 **CTFFIND5 runtimes**

360 To gauge the ability of CTFFIND5 to provide real time feedback during cryoEM data
361 collection we measured its runtime on three representative micrographs (Table 2).
362 Without estimation of tilt or sample thickness CTFIND5 performed CTF estimation roughly
363 within a second. Estimation of the sample thickness adds roughly half a second to the
364 runtime, therefore allowing CTF estimation within a timeframe comparable to typical
365 exposure times. Estimation of the tilt on the other hand increased runtimes substantially to
366 the order of several minutes, due to the exhaustive search of potential tilts over hundreds
367 of power spectra. While these runtimes are substantially slower than cryoEM data
368 acquisition, near real time estimation can be achieved by using multiple CPU cores.
369 Furthermore, optimization of the number of tiles used, better search algorithms, or

370 implementations employing GPUs could increase the speed to the point where real time
371 estimation is more feasible.

372 Conclusion

373 The new features implemented in CTFFIND5 improve CTF estimation from the power
374 spectra of cryoEM micrographs where assumptions made in its predecessor, CTFFIND4,
375 namely a thin and untilted sample, do not hold. The tilt of the sample is estimated by fitting
376 the CTF to the power spectra calculated from small patches across the image, similar to
377 other software including CTFTilt (Mindell and Grigorieff, 2003), Ctfplotter (Mastronarde,
378 2024; Xiong et al., 2009), goCTF (Su, 2019), Bsoft (Heymann and Belnap, 2007), and Warp
379 (Tegunov and Cramer, 2019). After estimation of the sample tilt, a tilt-corrected power
380 spectrum is produced that exhibits stronger Thon rings at higher resolution.

381 To take into account the modulation of the power spectra by thick samples (McMullan et
382 al., 2015; Tichelaar et al., 2020) we fit a modified CTF model, which increases the resolution
383 of the fitted regions of the spectra and provides a read-out of the sample thickness. While
384 the low exposures (3-5 $e^-/Å^2$) typically used in electron cryo-tomography often preclude
385 fitting of sample thickness from power spectra of individual images in the tilt series, we
386 demonstrate that this works reliably for higher exposures (~ 30 $e^-/Å^2$) typically used for
387 2D template matching (2DTM) (Lucas et al., 2021; Rickgauer et al., 2017) and in-situ single
388 particle analysis (Cheng et al., 2023).

389 We mainly developed these improvements for 2DTM applied to *in-situ* samples, e.g.,
390 prepared by cryo-FIB milling. Since the sample thickness and sample tilt are apparent from
391 a single exposure, as opposed to a reconstructed tomogram, CTFFIND5 made it possible to
392 quantify these parameters for every exposure. This is important information to judge the
393 quality of the lamella before performing time-intensive further processing (Lucas and
394 Grigorieff, 2023; Tuijtel et al., 2024). Furthermore, since the quality of fit estimation of
395 CTFFIND5 goes to higher resolution in tilted and thick samples (Fig. 1c, Fig. 3b-d) it is a
396 better indicator of micrograph quality than the same metric in CTFFIND4.

397 Even though we used tilt-series data to benchmark tilt estimation in CTFFIND5, there are
398 certain drawbacks in its use for tilt series data. In contrast to software optimized for tilt-
399 series data, such as Ctfplotter (Mastronarde, 2024), CTFFIND5 uses no prior information
400 for tilt axis angle and sample tilt, resulting in reduced performance and potential also lower
401 accuracy. Furthermore, there is no option to pool data from several tilt-angles to provide a
402 more accurate defocus or astigmatism estimation. However, this also means that CTFFIND5
403 together with fit_tilt_model might be useful in troubleshooting angle conventions in tilt
404 series data. Also, existing pipelines using CTFFIND4 might benefit from the tilt correction in
405 the powerspectrum calculation introduced in CTFFIND5, which results in more robust
406 defocus estimation at high tilt (Fig. 2).

407 While most single-particle samples are thin and flat and therefore do not benefit from
408 CTFFIND5, there might be some samples, such as viral particles (Fig. 3d), where direct
409 estimation of the ice thickness is valuable. However, even in these cases the defocus
410 reported by CTFFIND5 is an average for the whole micrograph and per-particle CTF
411 refinement, as implemented in *cis*TEM (Grant et al., 2018), RELION (Zivanov et al., 2018),
412 or CryoSPARC (Punjani et al., 2017; Zivanov et al., 2020) will be still be required to actually
413 recover high-resolution information during averaging. The ability to measure sample tilt
414 might be useful for approaches where a tilted stage is used to overcome preferred particle
415 orientation (Tan et al., 2017), as initial per particle defocus values can be derived from the
416 tilt as reported by CTFFIND5 and the particle positions.

417 In summary, the improvements implemented in CTFFIND5 result in more accurate CTF
418 estimation of thick and tilted samples and provide valuable information about the samples
419 to the microscopist.

420 Data availability

421 The images of tilted aquaporin crystals were previously published (Murata et al., 2000) and
422 are available at *https://grigoriefflab.umassmed.edu/tilted_aquaporin_crystals* . The untilted
423 exposures of ER-HOXB8 cells are available at EMPIAR (EMPIAR-11063). The tomograms
424 and tilt series from ER-HOXB8 cells have been deposited to EMDB (EMD-43419, EMD-
425 43420, EMD-43424, EMD-43425, EMD-43427, EMD-43428, EMD-43429) and EMPIAR

(EMPIAR-11854), respectively. The source code for CTFFIND5 is available at *https://github.com/timothygrant80/cisTEM/tree/ctffind5* and binaries for most Linux distributions can be downloaded at *https://cistem.org/development* .

Acknowledgments

We would like to thank members of the Grigorieff lab for testing CTFFIND5 and helpful discussion. We furthermore thank Benjamin Himes for helpful discussions and code review within *cis*TEM. We thank Alexis Rohou for comments on the manuscript. L.K. and N.G. gratefully acknowledge funding from the Chan Zuckerberg Initiative, grant #2021-234617 (5022).

Author contributions

Conceptualization: J.E. and N.G.; Data curation: J.E., L.K. and X.Z.; Formal analysis: J.E., L.K., X.Z. and N.G.; Funding acquisition: N.G.; Investigation: J.E., L.K. and X.Z.; Methodology: J.E., L.K. and N.G.; Project administration: J.E. and N.G.; Resources: J.E. and N.G.; Software: J.E., L.K. and N.G.; Supervision: J.E. and N.G.; Validation: J.E., L.K., X.Z. and N.G.; Visualization: J.E., L.K. and X.Z.; Writing – original draft: J.E., L.K., X.Z. and N.G.; Writing - review & editing: J.E., L.K., X.Z. and N.G.;

Tables

Table 1: Comparison of CTFFIND5 estimation of sample tilt with crystallographic analysis

Image	Axis angle φ			Tilt angle θ		
	crystallog.	ctffind5	$\Delta\varphi$	crystallog.	ctffind5	$\Delta\theta$
530394	93.28	94.98	-1.7	19.6	20.69	-1.09
530419	109.78	106.51	3.27	18.66	16.04	2.62
530430	104.38	101.13	3.25	21.32	20.37	0.95
530444	98.39	97.62	0.77	20.72	20.88	-0.16
660027	99.68	102.34	-2.66	19.4	22.39	-2.99
540149	94.45	85.84	8.61	43.08	44.59	-1.51
540291	96.16	98.1	-1.94	45.11	40.68	4.43

540302	93.98	93.39	0.59	44.7	44.21	0.49
540313	95.34	95.13	0.21	44.03	46.49	-2.46
660183	97.69	97.27	0.42	48.13	48.99	-0.86
550069	90.08	92.55	-2.47	60.46	60.83	-0.37
550089	91.48	92.04	-0.56	60.5	60.72	-0.22
660291	93.23	92.19	1.04	57.59	59.19	-1.60
660421	89.32	89.06	0.26	61.36	60.01	1.35
680341	89.67	90.02	-0.35	58.68	59.62	-0.94
530345	N/A	108.6		0	0.84	-0.84
530356	N/A	231.17		0	1.93	-1.93
530358	N/A	56.58		0	1.29	-1.29
530375	N/A	3.21		0	0.79	-0.79
530378	N/A	67.6		0	2.17	-2.17

446 **Table 2:** Runtime of CTFFIND5 on representative micrographs

Micrograph		1	2	3
Image properties				
Image size		4070x2892	2880x2046	4746x3370
Pixel size (Å)		1.5	4.175	2.5
Runtime (s)				
Tilt	Thickness			
-	-	0.9±0.1	0.7±0.1	1.7±0.1
+	-	39.0±0.2	208±1	173.4±0.1
-	+	1.4±0.1	1.3±0.1	2.4±0.1
+	+	39.5±0.1	209±1	173.0±0.1

447

Figures

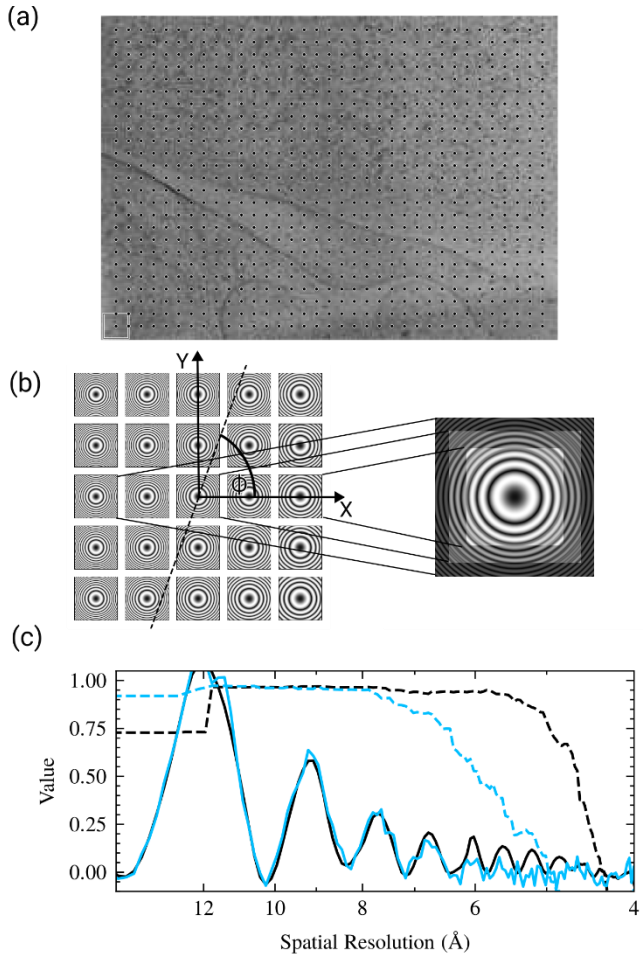

Figure 1: Tilt estimation and correction in CTFFIND5. (a) Power spectra are calculated in 128x128 pixel patches as indicated on a representative micrograph. The dots represent the locations of the patches and the box indicates patch size. (b) A model of the expected power spectrum in each patch given an average defocus Δf, tilt angle θ, and tilt axis ϕ is compared to the actual power spectra of tiles. After an optimal set of θ and ϕ has been found a corrected power spectrum is calculated by summing the tile power spectra, scaled to correct for the defocus difference. Power spectra shown are an exaggerated example. The convention of ϕ as a counterclockwise rotation from the x-axis is indicated. (c) Comparison of the original power spectrum (EPA, solid line, blue) to the tilt-corrected power spectrum (solid line, black). The tilt-corrected power spectrum exhibits clear peaks

at higher spatial resolution than the uncorrected power spectrum, as evident by the "goodness-of-fit" scores (dashed lines). The estimated CTF parameters are $\Delta f_1 = 10603$ Å, $\Delta f_2 = 10193$ Å, $\alpha = 85.9°$ for the uncorrected power spectrum and $\Delta f_1 = 10492$ Å, $\Delta f_2 = 10342$ Å, $\alpha = 81.2°$, $\theta = 12.3°$, $\phi = 261.6°$ for the tilt-corrected power spectrum. The fit resolution is 5.9 Å for the uncorrected power spectrum (dashed line, blue) and 4.6 Å for the tilt-corrected spectrum (dashed line, black).

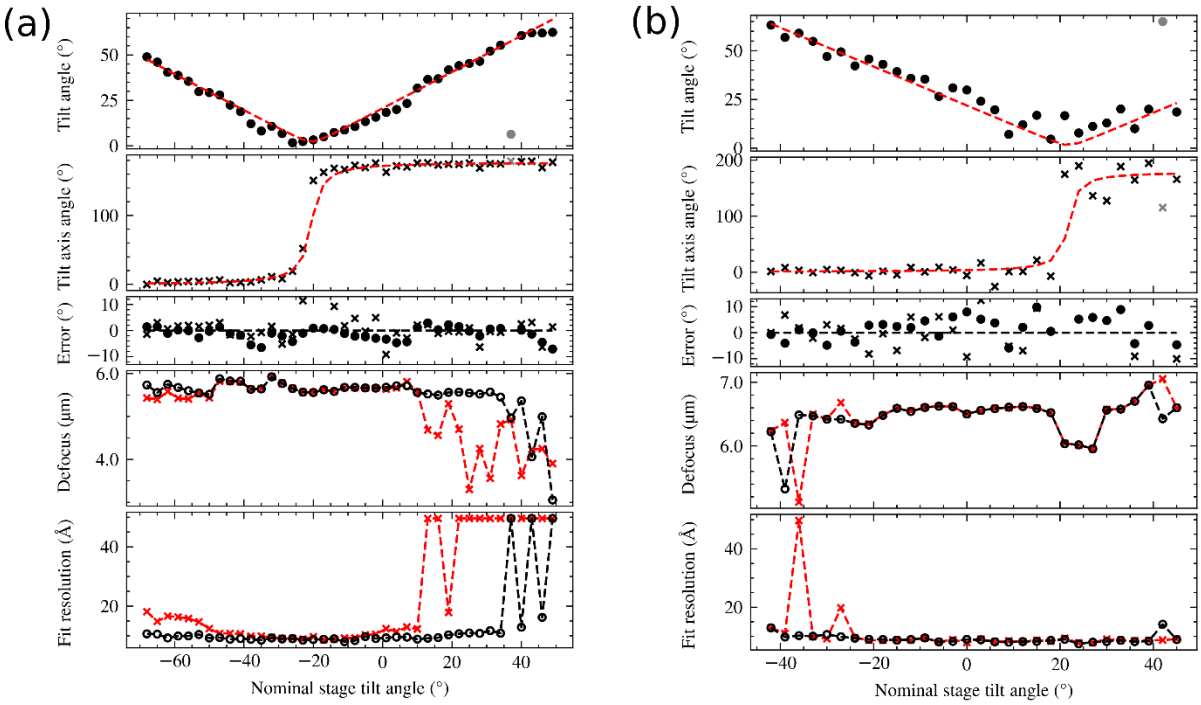

Figure 2 Validation of tilt estimation using tilt series data and comparison of defocus estimation using CTFFIND4 and CTFFIND5. (a) Estimated tilt angle and axis of 40 micrographs of a tilt series taken on a FIB-milled biological specimen. For each image the tilt angle (dots, top plot) and tilt axis direction (crosses, second plot) are plotted as a function of the nominal stage angle. The data were fitted to a model of the specimen tilt and constant stage tilt axis before tilting the stage (red dashed line in first and second plot). The estimated stage tilt axis has an angle of 178.2° and the estimated specimen pre-tilt is 20.6° with a tilt axis of 171.8°, which is consistent with the FIB-milling angle of 20° and manual alignment of the milling direction to the goniometer tilt axis. The third plot shows the fit residuals for tilt angle and axis are plotted. The fourth and fifth plot show a plot of the estimated defocus value and fit resolution for each tilt image, as derived from CTFFIND4 (red) or CTFFIND5 (black. (b) Data for another tilt series plotted as described for (a). The estimated stage tilt axis is 179.8°, the estimated specimen pre-tilt is -21.9° with a tilt axis of 183.8°. This is consistent with this grid being inserted in the opposite orientation as the grid shown in (a), but still with a rough alignment of milling direction and tilt axis.

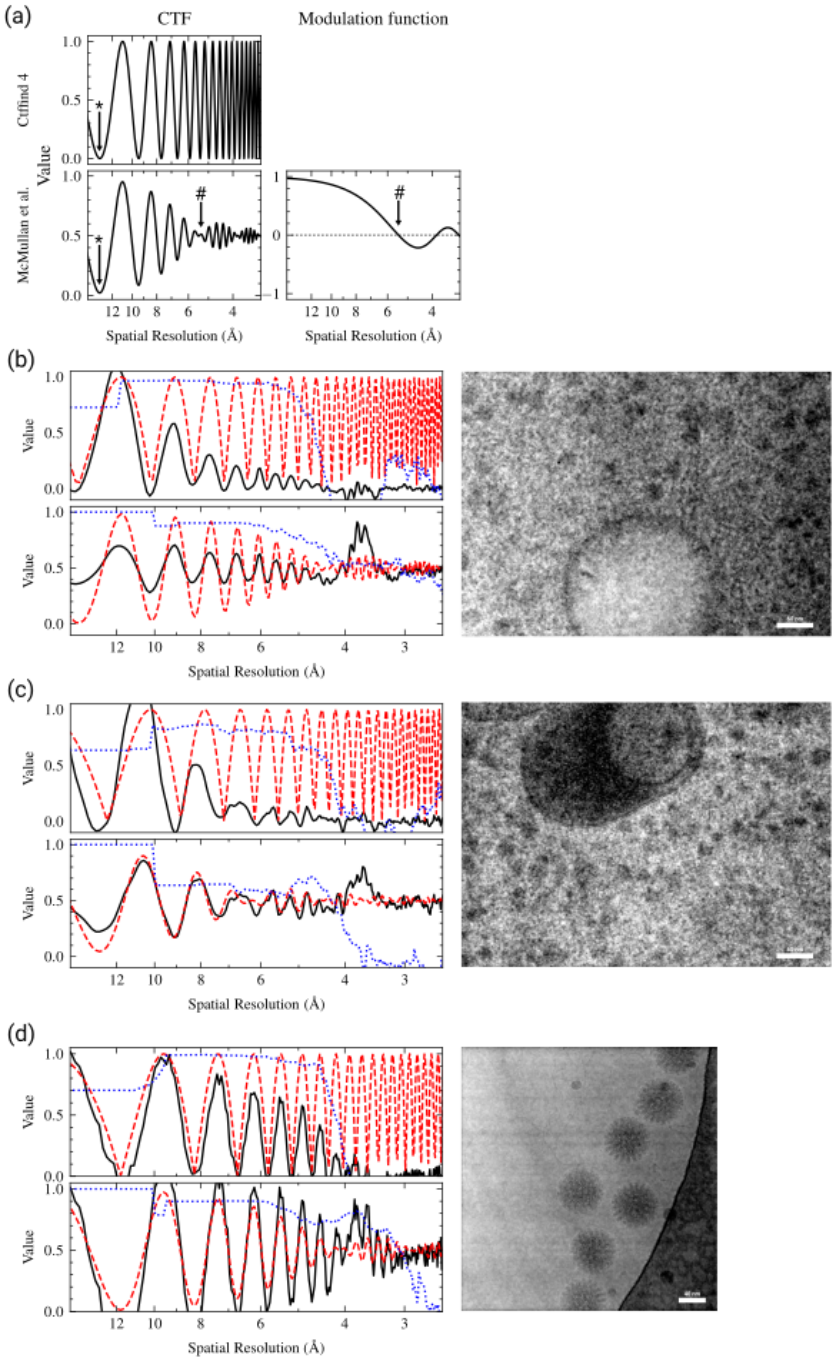

484

485 **Figure 3:** Sample thickness estimation by fitting Thon ring patterns. (a) Comparison of the
486 CTF model used in CTFFIND4, and after applying the modulation function (right) described
487 by *(McMullan et al., 2015)*. A star symbol (*) denotes the position of the first zero in the CTF
488 and a pound symbol (#) denotes the position of the first node. (b-d) Representative
489 examples of Thon ring fitting in micrographs without (top-left graph) and with (bottom-left

graph) thickness estimation. The micrograph is shown to the right. Each graph shows that EPA of the power spectrum in solid black lines, the fitted CTF model in dashed red lines, and the goodness of fit indicator as a dotted blue lines. (b) Thon ring fitting of a micrograph taken from a FIB-milling derived lamella. The tilt of the specimen was estimated to be 12.3°. When fitting without thickness estimation the estimated parameters were $\Delta f_1 = 10492$ Å, $\Delta f_2 = 10342$ Å, $\alpha = 81.2°$. When taking sample thickness into account the estimated parameters were $\Delta f_1 = 10481$ Å, $\Delta f_2 = 10286$ Å, $\alpha = 69.6°$, $t = 969$ Å. The estimated fit resolution was 4.6 Å and 3.4 Å without and with sample thickness estimation, respectively. (c) Thon ring fitting of a micrograph taken from a FIB-milling derived lamella. The tilt of the specimen was estimated to be 6.7°. When fitting without thickness estimation the estimated parameters were $\Delta f_1 = 8002$ Å, $\Delta f_2 = 7717$ Å, $\alpha = 73.4°$. When taking sample thickness into account the estimated parameters were $\Delta f_1 = 8549$ Å, $\Delta f_2 = 8343$ Å, $\alpha = 63.3°$, $t = 2017$ Å. The estimated fit resolution was 4.3 Å and 4.2 Å without and with sample thickness estimation, respectively. (d) Thon ring fitting of a micrograph taken from plunge frozen rotavirus double-layered particles *(Grant and Grigorieff, 2015)*. When fitting without thickness estimation the estimated parameters were $\Delta f_1 = 7027$ Å, $\Delta f_2 = 6808$ Å, $\alpha = -20.3°$. When taking sample thickness into account the estimated parameters were $\Delta f_1 = 7027$ Å, $\Delta f_2 = 6808$ Å, $\alpha = -22.9°$, $t = 850$ Å. The estimated fit resolution was 4.2 Å and 3.2 Å without and with sample thickness estimation, respectively.

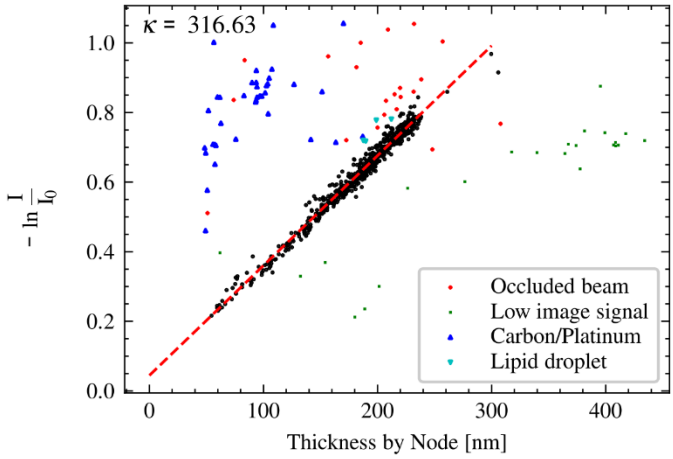

Figure 4: Validation of sample thickness estimation in CTFFIND5 by comparing the estimates to the intensity attenuation by the zero-loss energy filter. An estimation of the linear relationship using the RANSAC algorithm results in a slope of 1/316.6 nm and an x-axis intercept at -14 nm (red dashed line). Data points that were labeled as outliers by the RANSAC algorithm were manually inspected and color-coded according to visual inspection of the micrographs.

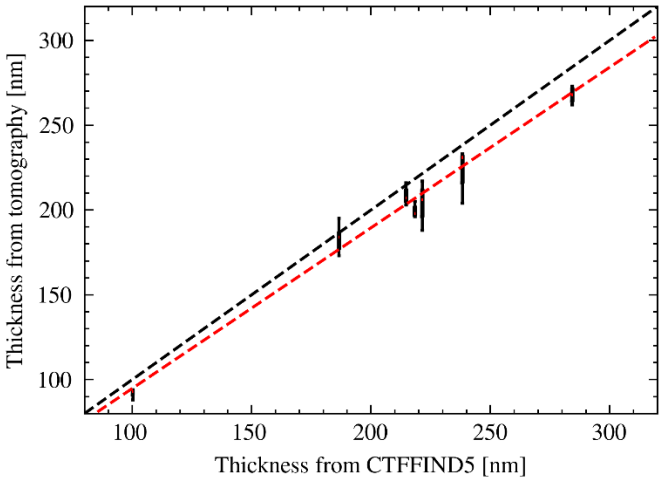

Figure 5: Validation of sample thickness estimation in CTFFIND5 by tomography. The distribution of thickness measurements in seven tomograms are shown as box plots with the median indicated by a red line. The position on the x-axis corresponds to the thickness estimate by CTFFIND5. The black dashed line indicates identity. The red dashed line indicates the result of a linear fit.

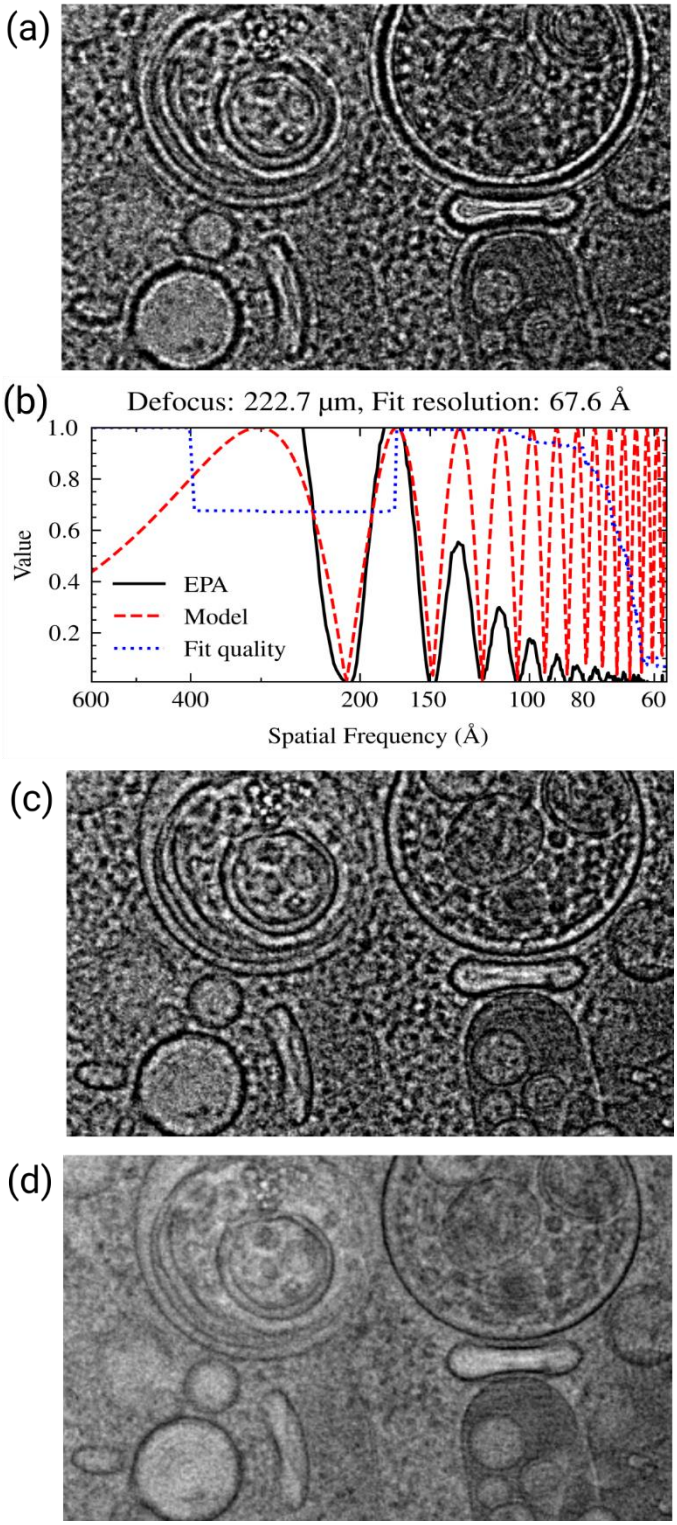

Figure 6: CTF correction of medium magnification overviews. (a) Representative area of a micrograph of a cellular sample at a pixel size of 40 Å without CTF correction. (b) Fit of the

power spectrum of the micrograph shown in panel a CTF model. (c-d) The same micrograph as shown in panel (a) after CTF correction by phase flipping (c) or with a Wiener-like filter (d). The custom fall-off parameter was set to 1.3 and the custom strength parameter was set to 0.7.

Bibliography

Cheng J, Liu T, You X, Zhang F, Sui S-F, Wan X, Zhang X. 2023. Determining protein structures in cellular lamella at pseudo-atomic resolution by GisSPA. *Nat Commun* **14**:1282. doi:10.1038/s41467-023-36175-y

Elferich J, Schiroli G, Scadden DT, Grigorieff N. 2022. Defocus Corrected Large Area Cryo-EM (DeCo-LACE) for label-free detection of molecules across entire cell sections. *Elife* **11**:e80980. doi:10.7554/eLife.80980

Grant T, Grigorieff N. 2015. Measuring the optimal exposure for single particle cryo-EM using a 2.6 Å reconstruction of rotavirus VP6. *eLife* **4**:e06980. doi:10.7554/eLife.06980

Grant T, Rohou A, Grigorieff N. 2018. cisTEM, user-friendly software for single-particle image processing. *Elife* **7**:e35383. doi:10.7554/eLife.35383

Hagen WJH, Wan W, Briggs JAG. 2017. Implementation of a cryo-electron tomography tilt-scheme optimized for high resolution subtomogram averaging. *Journal of Structural Biology*, Electron Tomography **197**:191–198. doi:10.1016/j.jsb.2016.06.007

Heymann JB, Belnap DM. 2007. Bsoft: image processing and molecular modeling for electron microscopy. *J Struct Biol* **157**:3–18. doi:10.1016/j.jsb.2006.06.006

Lucas BA, Grigorieff N. 2023. Quantification of gallium cryo-FIB milling damage in biological lamellae. *Proceedings of the National Academy of Sciences* **120**:e2301852120. doi:10.1073/pnas.2301852120

Lucas BA, Himes BA, Xue L, Grant T, Mahamid J, Grigorieff N. 2021. Locating macromolecular assemblies in cells by 2D template matching with cisTEM. *eLife* **10**:e68946. doi:10.7554/eLife.68946

Mastronarde DN. 2024. Accurate, automatic determination of astigmatism and phase with Ctfplotter in IMOD. *J Struct Biol* **216**:108057. doi:10.1016/j.jsb.2023.108057

Mastronarde DN. 2005. Automated electron microscope tomography using robust prediction of specimen movements. *J Struct Biol* **152**:36–51. doi:10.1016/j.jsb.2005.07.007

Mastronarde DN. 1997. Dual-Axis Tomography: An Approach with Alignment Methods That Preserve Resolution. *Journal of Structural Biology* **120**:343–352. doi:10.1006/jsbi.1997.3919

Mastronarde DN, Held SR. 2017. Automated tilt series alignment and tomographic reconstruction in IMOD. *J Struct Biol* **197**:102–113. doi:10.1016/j.jsb.2016.07.011

McMullan G, Vinothkumar KR, Henderson R. 2015. Thon rings from amorphous ice and implications of beam-induced Brownian motion in single particle electron cryo-microscopy. *Ultramicroscopy* **158**:26–32. doi:10.1016/j.ultramic.2015.05.017

Mindell JA, Grigorieff N. 2003. Accurate determination of local defocus and specimen tilt in electron microscopy. *J Struct Biol* **142**:334–347. doi:10.1016/s1047-8477(03)00069-8

Murata K, Mitsuoka K, Hirai T, Walz T, Agre P, Heymann JB, Engel A, Fujiyoshi Y. 2000. Structural determinants of water permeation through aquaporin-1. *Nature* **407**:599–605. doi:10.1038/35036519

Pedregosa F, Varoquaux G, Gramfort A, Michel V, Thirion B, Grisel O, Blondel M, Prettenhofer P, Weiss R, Dubourg V, Vanderplas J, Passos A, Cournapeau D, Brucher M, Perrot M, Duchesnay E. 2011. Scikit-learn: Machine Learning in Python. *Journal of Machine Learning Research* **12**:2825–2830.

Punjani A, Rubinstein JL, Fleet DJ, Brubaker MA. 2017. cryoSPARC: algorithms for rapid unsupervised cryo-EM structure determination. *Nat Methods* **14**:290–296. doi:10.1038/nmeth.4169

Rice WJ, Cheng A, Noble AJ, Eng ET, Kim LY, Carragher B, Potter CS. 2018. Routine Determination of Ice Thickness for Cryo-EM Grids. *J Struct Biol* **204**:38–44. doi:10.1016/j.jsb.2018.06.007

Rickgauer JP, Grigorieff N, Denk W. 2017. Single-protein detection in crowded molecular environments in cryo-EM images. *eLife* **6**:e25648. doi:10.7554/eLife.25648

Rohou A, Grigorieff N. 2015. CTFFIND4: Fast and accurate defocus estimation from electron micrographs. *J Struct Biol* **192**:216–221. doi:10.1016/j.jsb.2015.08.008

Su M. 2019. goCTF: Geometrically optimized CTF determination for single-particle cryo-EM. *Journal of Structural Biology* **205**:22–29. doi:10.1016/j.jsb.2018.11.012

Tan YZ, Baldwin PR, Davis JH, Williamson JR, Potter CS, Carragher B, Lyumkis D. 2017. Addressing preferred specimen orientation in single-particle cryo-EM through tilting. *Nat Methods* **14**:793–796. doi:10.1038/nmeth.4347

Tegunov D, Cramer P. 2019. Real-time cryo-electron microscopy data preprocessing with Warp. *Nat Methods* **16**:1146–1152. doi:10.1038/s41592-019-0580-y

Thon F. 1971. Phase contrast transfer functionElectron Microscopy in Material Science. Academic Press New York. pp. 570–625.

Tichelaar W, Hagen WJH, Gorelik TE, Xue L, Mahamid J. 2020. TEM bright field imaging of thick specimens: nodes in Thon ring patterns. *Ultramicroscopy* **216**:113023. doi:10.1016/j.ultramic.2020.113023

Tuijtel MW, Cruz-León S, Kreysing JP, Welsch S, Hummer G, Beck M, Turoňová B. 2024. Thinner is not always better: Optimizing cryo-lamellae for subtomogram averaging. *Science Advances* **10**:eadk6285. doi:10.1126/sciadv.adk6285

Xiong Q, Morphew MK, Schwartz CL, Hoenger AH, Mastronarde DN. 2009. CTF determination and correction for low dose tomographic tilt series. *Journal of Structural Biology* **168**:378–387. doi:10.1016/j.jsb.2009.08.016

Yan R, Edwards TJ, Pankratz LM, Kuhn RJ, Lanman JK, Liu J, Jiang W. 2015. Simultaneous determination of sample thickness, tilt, and electron mean free path using tomographic tilt images based on Beer-Lambert law. *J Struct Biol* **192**:287–296. doi:10.1016/j.jsb.2015.09.019

Zhang K. 2016. Gctf: Real-time CTF determination and correction. *Journal of Structural Biology* **193**:1–12. doi:10.1016/j.jsb.2015.11.003

Zivanov J, Nakane T, Forsberg BO, Kimanius D, Hagen WJ, Lindahl E, Scheres SH. 2018. New tools for automated high-resolution cryo-EM structure determination in RELION-3. *Elife* **7**:e42166. doi:10.7554/eLife.42166

Zivanov J, Nakane T, Scheres SHW. 2020. Estimation of high-order aberrations and anisotropic magnification from cryo-EM data sets in RELION-3.1. *IUCrJ* **7**:253–267. doi:10.1107/S2052252520000081